Topography studies of concrete abraded with ice

Guzel Shamsutdinova[1], Max A.N. Hendriks, Stefan Jacobsen

[a]Norwegian University of Science and Technology, Department of Structural Engineering, Richard Birkelandsvei 1A, 7491, Trondheim, Norway
[b]Delft University of Technology, Faculty of Civil Engineering and Geosciences, Stevinweg 1 2628 CN Delft, the Netherlands

Abstract

Topography studies of concrete-ice abrasion were made to proceed in our understanding of the mechanisms of concrete wear by ice on Arctic offshore structures. The effects on various initial surfaces of a B75 normal-weight concrete (smooth, rough, sawn) and on the sawn surface of a LB60 lightweight concrete were studied during concrete-ice abrasion experiments. The degradation of a concrete surface appears mainly as valley formation resulting from air voids opening, or aggregate protrusion and cutting of peaks. The various initial roughness conditions were found to lead to an evolution with both increasing (at both meso- and microscale) and converging roughness. Protrusions from both lightweight and normal-weight aggregates were observed on sawn surfaces. Greater abrasion is seen on lightweight concrete and its initial roughness was much affected by the porous aggregate.

1. Introduction

Ice is known as an abrasive material in many fields. There are examples of negative abrasive effects, such as the erosion of coasts by glaciers or fast ice [1], the wear of winter sport equipment [2], risks for vessels operating in ice-covered seas [3], and damage to concrete structures (lighthouses, gravity-based structures for the oil industry, bridge piles) from the drifting ice in the Arctic and in the northern rivers. The degradation of concrete surfaces due to ice is known as concrete-ice abrasion. This topic has been studied over the last 40 years through both field observations [4–7] and laboratory studies [4,8–12]. The mechanics of the problem have also been investigated in reviews and using modelling [13]. High local ice pressure combined with the low tensile stress of concrete, 3-body wear, water pressure in cracks, and fatigue can all contribute to the wear of hard concrete by the softer ice. A pilot lattice model for the onset of wear based on Hertzian contact stress [14] was developed showing that ice contact can crack concrete.

Early studies of concrete-ice abrasion focused mainly on concrete and ice properties like temperature and ice pressure and less on the surface properties of concrete. It is known that concrete with higher compressive strength is less abraded [11,12,15].

An earlier part of this study found that the abrasion of high-performance concrete after 3 km of effective sliding distance was in the order of 0.1 mm, and the majority of the surface damage was observed during the first sliding kilometre [15]. This was interpreted as severe abrasion of concrete during the running-in process of sliding experiments from 0 to 1 km, which was followed by mild wear (steady state) over the distance from 1 to 3 km, where abrasion rates were much smaller [15]. The difference in abrasion rates could not be explained by the coefficient of friction (COF). Earlier testing of high-performance concrete with standard wear tests also showed severe-mild wear transitions [16], though this was not explained.

The importance of studying the effect of concrete surface parameters on abrasion has been highlighted previously [7,10,17]. Increasing concrete-ice abrasion was associated with increased surface roughness, and the number and size of asperities was related to contact stresses. The current research therefore focused on the material properties of concrete and its surface characteristics.

Fiorio carried out a systematic experimental study of concrete roughness effects on concrete-ice abrasion [10]. The tests were performed on mortar plates. The mortar had a very high water–cement ratio, w/c = 0.6, and used only fine aggregate (sand), so the compressive strength was 5 times lower than offshore concrete and the bond strength of cement paste to fine aggregate was weak. Two initial arithmetic average roughness R_a (0.11 and 0.28 mm) were created on moulded surfaces. The abrasion was higher for plates with the higher roughness. Other wear studies of various materials also explain the running-in process by an initially rough surface when the contact area is small and the load distribution therefore gives high local contact stresses [18–22].

An indirect study of roughness on concrete-ice abrasion can be found in Huovinen [4], where the concrete surface had protruding coarse aggregates (6–32 mm) due to both concrete-ice abrasion and freeze-thaw deterioration. The protruding stones were found to destroy ice, but the bond strength of cement paste to aggregate was reduced significantly by frost damage, and this caused aggregate particles from the concrete surface to detach.

The effect of surface parameters on wear is usually studied through the average roughness (microscale) and skewness. Although higher roughness causes greater wear during the running-in process [10,18], the effects of initial surface roughness on overall wear seem to vary. Some studies show that roughness decreases during the wear process [21,23] due to cutting of the peaks. Another study showed that high initial roughness decreased, while the lowest initial roughness increased during the test [24]. Liang et al. [18] concluded that there is a lower limit for roughness values, beyond which a further decrease has no effect on wear.

The skewness of the surface roughness was found to decrease during the wear test, and become more negative [20,21,23,25], i.e. the surface increasingly has more valleys than peaks. The surface with the highest resistance to wear has low roughness and high negative skewness. Such a surface is created during the running-in process; it has a high contact area and low COF [20,21].

The scope of this research is to investigate the severe-mild transition during concrete-ice abrasion tests with the help of surface topography studies. We

therefore study how the abrasion of three different initial concrete surfaces (mould, sawn, rough) of HPC (high performance concrete) developed under ice sliding and then analysed how surface roughness parameters were affected. We also investigate the roughness of a few samples at sub-microscale with a new-generation 3D optical microscope, study the protrusion of lightweight versus normal density aggregates, and characterize the wear debris of ice and concrete to increase our understanding of how concrete-ice abrasion works at various size scales.

2. Experiments

We investigated the abrasion of four different types of concrete surface exposed to sliding ice. The experiments included the production of concrete specimens and ice, the concrete-ice abrasion tests, the scanning of concrete surfaces, and the study of wear particles from both concrete and ice surfaces.

2.1. Concrete-ice abrasion experiments

The concrete-ice abrasion experiments were carried out in the department of Structural Engineering at the Norwegian University of Science and Technology (NTNU). The experimental conditions: ice pressure, temperature and velocity are chosen based on previous studies of concrete-ice abrasion [11]. The experiments took place in a cold laboratory. The cooling system is installed in the roof of the lab and generates cold air. The control unit maintains the target average air temperature of −10 °C ± 0.7 °C. The method simulates the sliding of fresh-water ice samples on concrete surfaces with a pressure of 1 MPa and an average sliding velocity of 0.16 m/s (Fig. 1). The concrete samples were small slabs with dimensions 100 × 310 mm and 50 mm high. The ice samples had a cylindrical shape with a concrete contact diameter of 73.4 mm and a height of 180 mm. The sliding distance for each concrete sample was 3 km. The temperature of the concrete sample is controlled through the aluminium heating plate below the concrete sample. The heating plate prevents icing on the concrete surface. From experience with our experimental set-up we know that an ice layer on the concrete surface prevents the abrasion, so it has to be ice free. The heating plate has a channel inside, connected at both ends to a controlled temperature liquid (alcohol) circulator. The temperature of the concrete surface during the test is approximately −2 °C (measured with an infrared thermometer), which is sufficient to keep the surface ice free during ice movement.

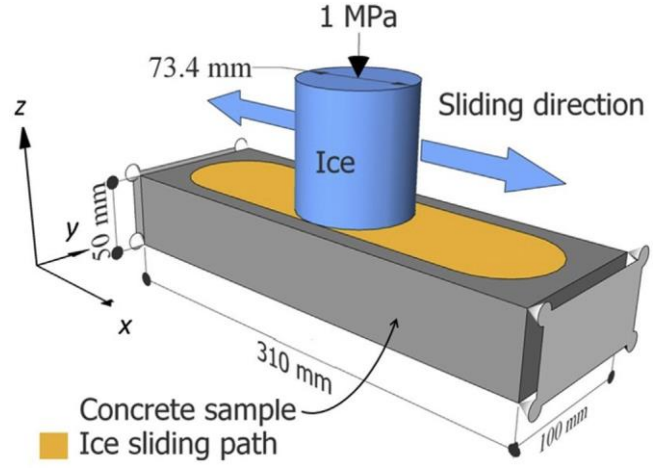

Fig. 1. Simplified diagram of the concrete-ice abrasion experiment.

2.2. Scanning of concrete surface

We scanned the concrete surfaces using a laser measurement method developed at the department, which measured the surfaces at four different stages of each concrete-ice abrasion test: the initial surface, and after each sliding kilometre. The set-up includes three components: the laser sensor itself, a linear motion system controlled by accompanying software, and finally a computer with a logger for data acquisition. These three components are synchronized with optimized scanning parameters (velocity and frequency). The laser sensor moves along the concrete surface with velocity of 10 mm/s, and measures heights (z-direction) at a logging frequency at 200 Hz. The diameter of the laser beam is approximately 50 μm. We verified the calibration of the laser sensor with a standard steel calibration block 2.5 mm thick and found to have a vertical accuracy of 16 μm. The measuring range of the laser in the z-direction is 10 mm.

The scanned region measures 95 mm in the y-direction by 299 mm in the x-direction, resulting in a matrix of surface heights with dimensions 1900 × 300 points, so that the measuring point distance is 1 mm in the x-direction and approximately 50 μm in the y-direction, cf. Fig. 2(a). Fig. 2 shows a simplified scheme of the measurement process. Since the measurements are denser in y-direction, we identify them as profiles (Fig. 2(a)), and the distance between two parallel 100 mm long profiles was 1 mm, for all samples during the measurements. Only for obtaining a higher scan image quality (like in Figs. 4, 8(b), and 13) the distance between two profiles was reduced to 0.1 mm. The scanning method and equipment are described in more detail in our previous paper [26].

Although the topography of the concrete surface was within the measurement range of the laser, there were measurement faults in the surface matrix. These faults were identified as sharply pronounced spikes on the scan result. Often, these spikes were observed at the edges of air-voids, presumably because the laser beam was blocked by the edge either on the way into the inner void or on the way out (hidden surface effects). Macro air-voids in hardened concrete (compaction voids) have irregular shapes and varying degrees of hidden inner surface under the sawn surface. These positive spikes were filtered out in a two-step procedure. Firstly, a one-dimensional median filter (200^{th} order) was applied to the raw data of each profile. Secondly, the raw data was compared with the filtered data, and where the raw data of a measuring point was 0.05 mm greater than the filtered profile, it was replaced locally with the filtered data (Fig. 3). The filtering out of negative spikes was rejected, because it would obscure the air-voids in the concrete surface. The amount of data filtered out varied from 0.5% (for smooth surfaces) up to 6.1% (for rough surfaces) of the total number of points in the surface matrix (approximately 585000).

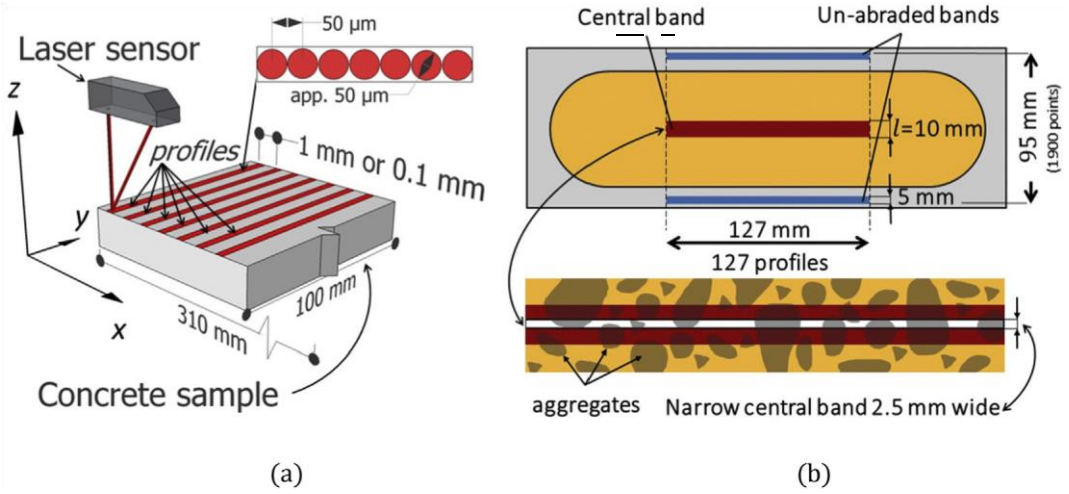

Fig. 2. (a) Simplified schematic of measurement process (not to scale); (b) simplified schematic of the different zones on the concrete surface.

The abrasion depth was calculated from the difference between the surrounding un-abraded band on the edges of the concrete sample and the central band of concrete, cf. Fig. 2 (b). The central band accumulated the maximum ice sliding distance on the concrete surface due to the cylindrical shape of the ice sample, so that a point on the concrete surface in this area experiences the longest ice movement. The average abrasion was found as the average value of the abrasion in the central band, which is 127 mm long and consists out of 127 central profiles; cf. Fig. 2 (b).

The roughness parameters, such as arithmetic average roughness (R_a), skewness (R_{sk}), kurtosis (R_{ku}), and the amplitude distribution function, were found within the central band (Fig. 2 (b)). The roughness parameters were calculated in accordance with ISO 4287 [27], using the following equations:

$$R_a = \frac{1}{l}\int_0^l |Z(y)|\,dy \quad (1)$$

$$R_q = \sqrt{\frac{1}{l}\int_0^l Z(y)^2 dy} \quad (2)$$

$$R_{sk} = \frac{1}{R_q^3}\left[\frac{1}{l}\int_0^l Z\,y\,dy()^3\right] \quad (3)$$

$$R_{ku} = \frac{1}{R_q^4}\left[\frac{1}{l}\int_0^l Z\,y\,dy()^4\right] \quad (4)$$

where z is the surface height and l is the width of the central band, 10 mm.

The separate study of the abrasion of aggregate particles and cement paste or mortar was done within the narrow central band of 2.5 mm (Fig. 2(b)), because at this width it was possible to sort the profiles and manually pick which of them belonged to aggregates and which to the mortars. Approximate sizes of aggregate particles within this narrow central band were 7–19 mm for lightweight concrete and 9–15 mm for normal-weight concrete.

A few surface measurements down to sub-microscale were made with a 3D optical microscope (Bruker, ContourGT-K) in the Nanolab at NTNU. The sawn surface of lightweight concrete was scanned before and after the concrete-ice abrasion test. The measurement area was small (approx. 10 by 15 mm).

2.3. Concrete mixes and surfaces

To examine the effect of concrete surface roughness on the abrasion process, we used four different types of concrete surface (Fig. 4). Three types of concrete surface were prepared from one concrete mix (B75): sawn, moulded and sandblasted. Each test was repeated once, so there are two parallel samples of each type. Moulded samples (labelled as MB75) have a relatively smooth cement paste surface; the mould form

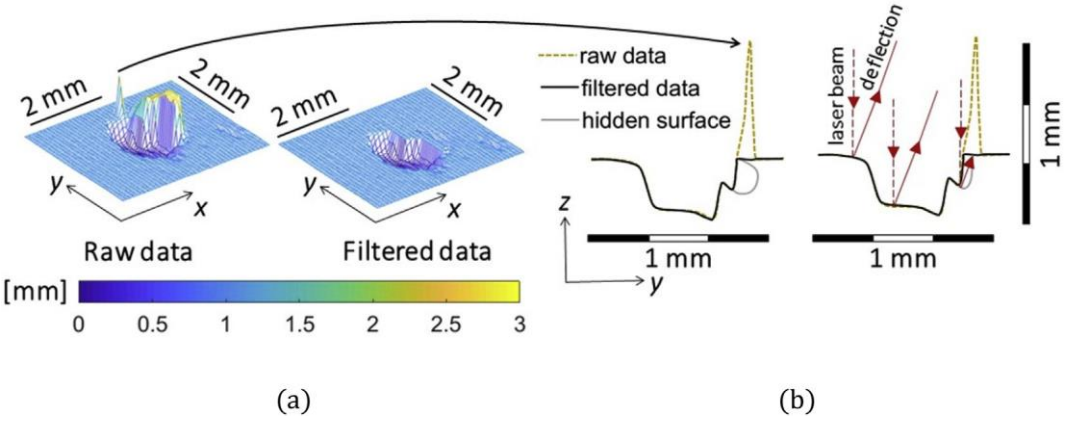

Fig. 3. Example of raw data, and data after filtering: (a) surface matrix with raw and filtered data; (b) profile of raw and filtered data with examples of hidden surface and blocked laser deflection.

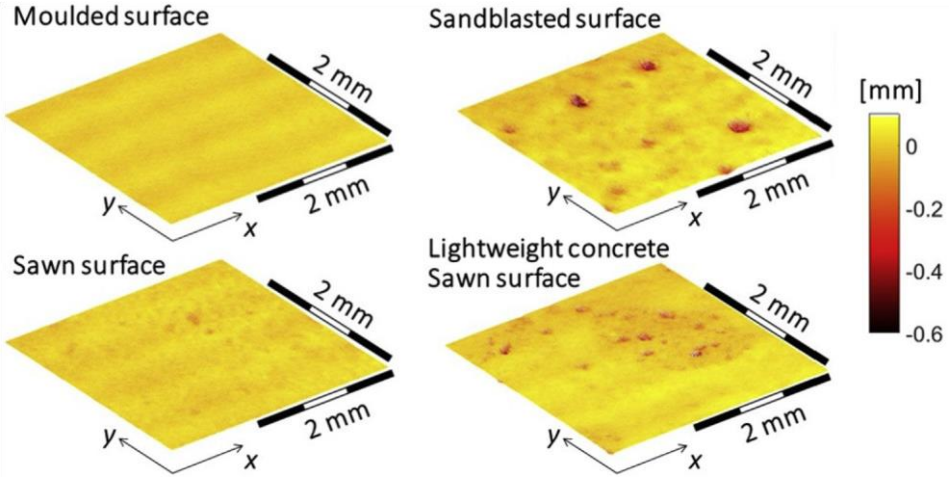

Fig. 4. Typical concrete surfaces before testing.

was steel. Sandblasted samples (labelled as BB75) were made by dry sandblasting moulded surfaces with AlSiO4 (1–2 mm). The resulting surface was relatively rough and has cement paste with fine aggregates (crushed gravel, 0–8 mm grain size) and open air-voids. Sawn-concrete samples (labelled as SB75) were made by wet sawing with a diamond saw blade 2.5 mm thick, and then grinding away visual traces of the saw with the side of the diamond sawblade afterwards. This surface is relatively smooth with cut-through cement paste, fine and coarse (crushed gravel, 8–16 mm grain size) aggregates, and air-voids. These three types of surface allowed us to look at the abrasion of a smooth top cement paste layer, rough non-homogenous surfaces with fine aggregates, and smooth non-homogenous surfaces with fine and coarse aggregates.

Since the concrete mixes have an aggregate volume fraction of 72%

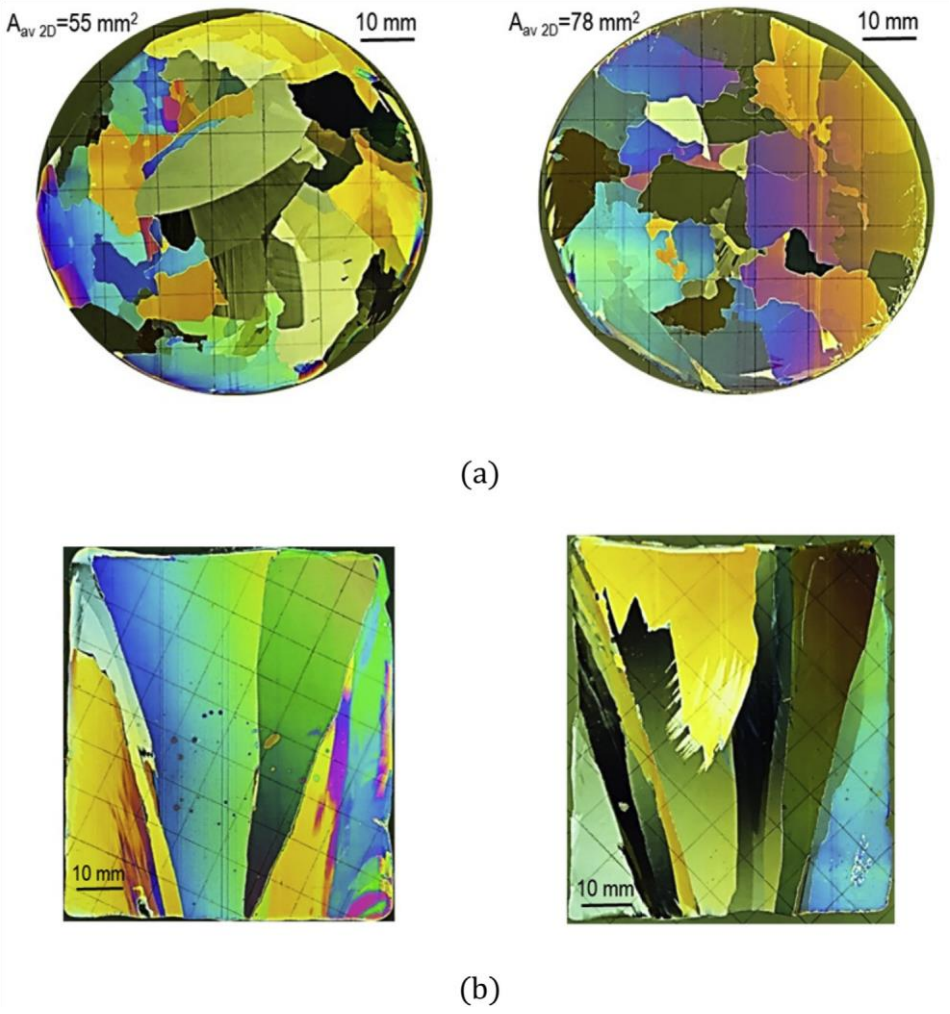

Fig. 5. Thin sections of typical ice samples (a) horizontal cross section (30 mm above the contact with concrete); (b) vertical cross section (contact line at the top).

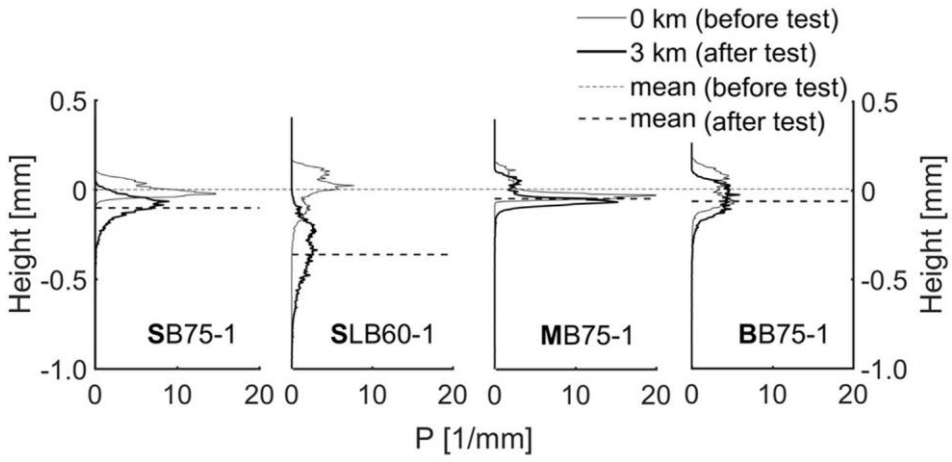

Fig. 6. Amplitude distribution functions for four different concrete surfaces.

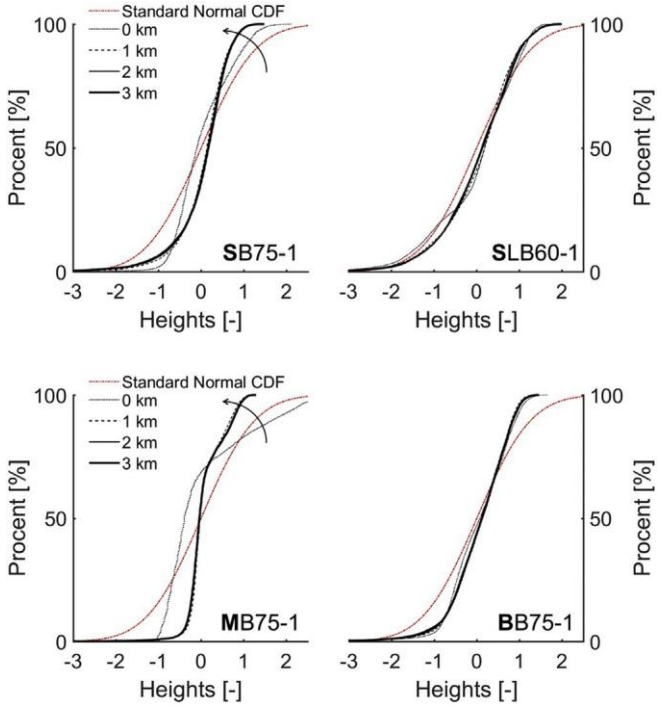

Fig. 7. Normalized amplitude distribution functions and the standard distribution function.

(B75 mix), the surface fraction of aggregate particles is considerably higher than fraction of the cement paste. To examine the behaviour of other types of coarse aggregate on the abrasion of concrete, sawn samples of lightweight concrete (LWC) (labelled as SLB60) were included in the experimental programme. The lightweight concrete mix has a porous coarse aggregate with lower density (1530 kg/m^3) than normal-weight aggregate (2690 kg/m^3). Nowadays there is a lot of interest in lightweight concrete for structures, especially offshore structures.

Table 1 shows the properties of the fresh concrete mixes, cube compressive strength and labels of the samples tested. The fresh concrete properties were determined in accordance with EN 12350 [28]. The samples were classified in accordance with NS-EN
206:2013+NA:2014 [29].

2.4. Fresh-water ice as abrasive material

In these experiments, the concrete surface is abraded by fresh-water ice produced by unidirectional freezing. The density of the ice is 917.0 kg/m^3, so its porosity is very low: 0.1–0.0033% [15]. The method of ice production is described in detail in our previous paper [26].

To investigate the ice structure, thin sections of ice were cut using a microtome. Fig. 5 shows that a typical ice sample consists of columnar ice grains. The average grain size in horizontal cross section (approximately 30 mm above the bottom of the ice cylinder, at the same time 30 mm above the contact with the concrete surface) was measured as an area fraction based on the 2D image of two different thin sections. This showed the average 2D size of ice grains was 55 mm^2 in one section and 78 mm^2 in the other.

2.5. Ice and concrete wear particles

Earlier research using the concrete-ice abrasion test showed that the wear of ice is 30,000–100,000 times greater than the wear of concrete [15]. The ice can change into water through melting, or into slush ice or ice fragments [26]. The ice fragments were here interpreted as ice wear particles. The ice fragments were collected during concrete-ice abrasion tests on sawn surfaces after three ice samples had been consumed. During the abrasion testing, they were deposited on the side of the concrete sample on plastic foil. A total of 433 g of ice fragments were collected and sieved in a similar manner as in Timco and Jordaan [30], though the screen opening was larger. The sieves were: < 2 mm, 2–4 mm, 4–8 mm, and > 8 mm.

Concrete wear particles were also collected during concrete-ice abrasion tests on sawn surfaces, separately for the two concrete mixes, B75 and LB60. The concrete surface was rinsed with water after (approximately) every 0.1–0.3 km of sliding distance. This water was filtered afterwards with filter paper (pore size: 12–25 μm). The concrete wear particles collected were studied with the optical microscope.

3. Results

3.1. Amplitude distribution function

Fig. 6 shows amplitude distribution functions for the four concrete surfaces before and after 3 km of concrete-ice abrasion testing. The difference between the two lines (initial and final distributions) illustrates the abrasion of the surface. The dashed lines show the mean distributions.

The width of the distribution shows its unevenness and roughness. Sample MB75-1 has the narrowest initial height distribution, which corresponds to the visual impression of a smooth surface in Fig. 4. In contrast, sandblasted sample (BB75-1) shows the widest amplitude distribution, which corresponds to the greatest roughness in Fig. 4. Of the two sawn samples, the lightweight concrete mix SLB60-1 has the widest distribution, which can be explained by the high air-void content of the concrete mix (Table 1) and the high porosity of the aggregate, which increased roughness much more than the granite aggregate in SB75-1.

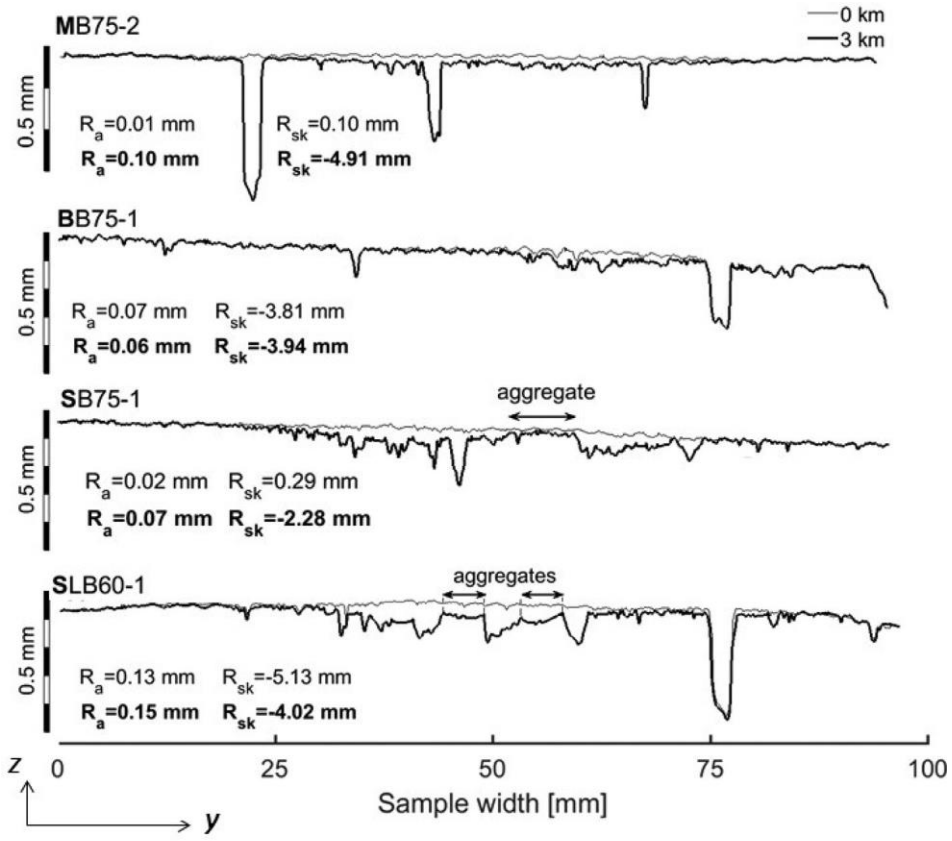

(a)

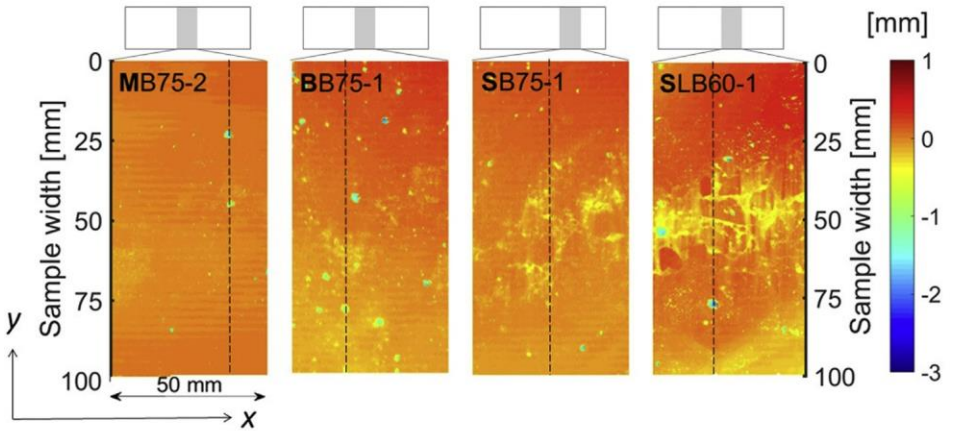

(b)

Fig. 8. (a) Profiles of concrete surface before and after 3 km of concrete-ice abrasion testing; (b) the 50 mm width of the corresponding concrete surface after 3 km of testing (the dashed lines indicate the position of the profiles in a), and the inserts above the surfaces indicate the position of the profiles on the concrete surface.

Fig. 7 shows normalized cumulative amplitude distribution functions and the standard distribution function of the central band for the four concrete surfaces before the test and after each kilometre of concrete-ice abrasion. These are often called bearing-curves in wear testing. A normality test was rejected for all surfaces.

3.2. Surface degradation

Fig. 8 (a) shows profiles for the four types of concrete surface before and after 3 km of concrete-ice abrasion testing. Fig. 8 (b) shows the 50 mm width of corresponding concrete surface after 3 km of testing, with the dashed line indicating the profile location.

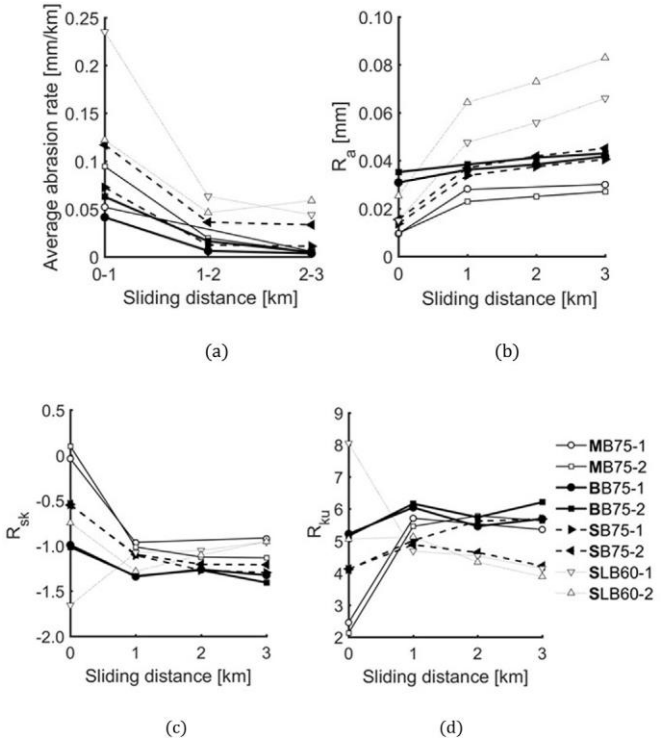

Fig. 9. (a) Average abrasion rates of concrete during the tests; (b) average roughness of concrete surfaces; (c) skewness of concrete surfaces; (d) kurtosis of concrete surfaces with the sliding distance.

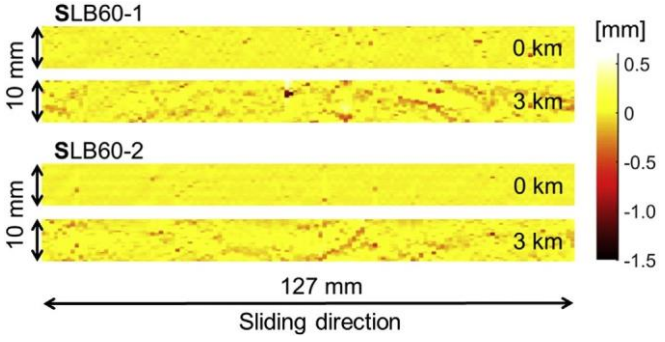

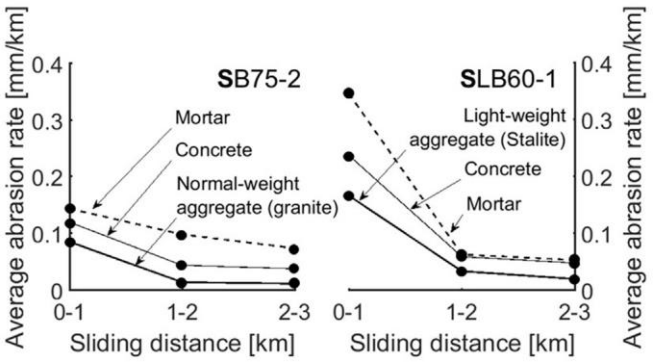

Fig. 12. Abrasion rate of mortar, coarse aggregates (granite and LWA) and concrete.

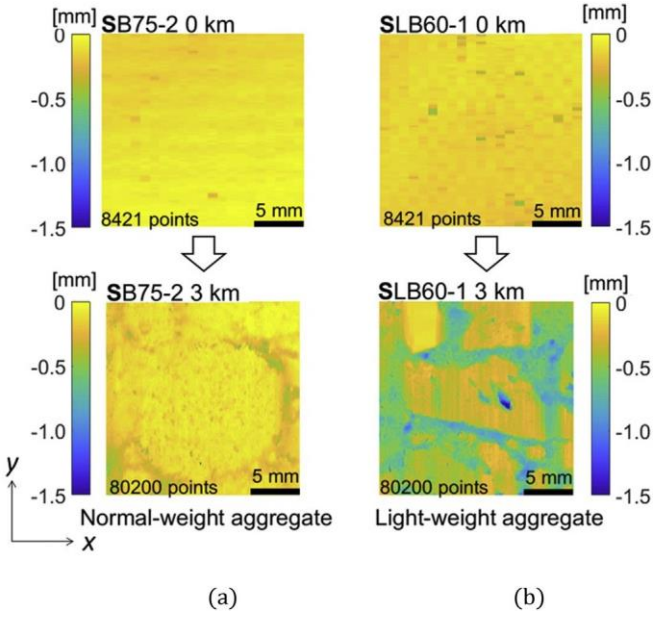

Fig. 13. Parts of the surface scan before and after 3 km testing: (a) normalweight aggregate; (b) lightweight aggregate. (Note: the resolution for scans before the test was lower than for scans after the test.)

Fig. 10. Topography of the central band before and after 3 km testing for two parallel samples SLB60 (the central band has 25400 points).

Fig. 8 (a) shows profiles of concrete surfaces at right angles to the ice sliding direction, which means that the abrasion of concrete was in the centre of these profiles. Along the edges, at 0 and 100 mm on the vertical scale in Fig. 8(b), no ice was in contact with concrete, so this is the un-abraded reference surface.

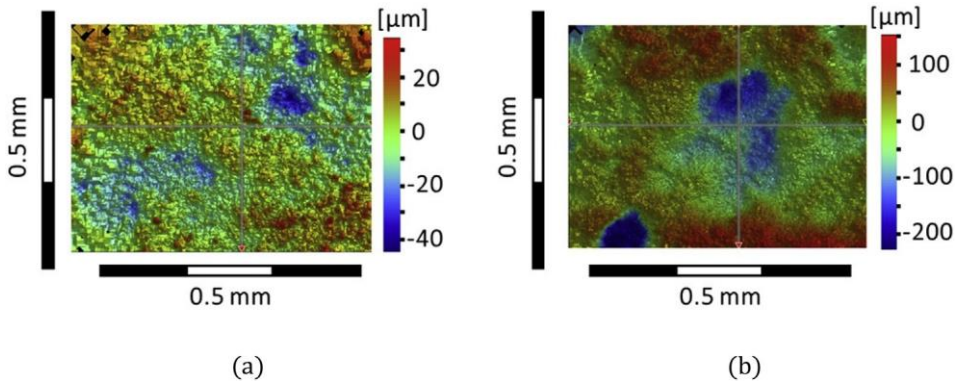

Fig. 11. Scan of sawn lightweight concrete (LB60) with 3D optical microscope: (a) before the test; (b) after 3 km testing. (Note: the vertical colour scale is different.).
(For interpretation of the references to colour in this figure legend, the reader is referred to the Web version of this article.)

Table 1
Concrete properties of tested mixes.

	B75	LB60
W/(C+2S)*	0.42	0.40
Density, kg/m^3	2455	1905
Air content, %	0.9	6.7
Slump measure, mm	200	195
Slump spread measure, mm	420	410
Coarse aggregate	Årdal 8–16 mm (50%), crushed gravel	Stalite ½″ (23%) and ¾″(23%), lightweight aggregate
Fine aggregate	Årdal 0–8 mm (50%), natural sand	Årdal 0–8 mm (54%), natural sand
28-day compressive strength (cube), MPa	90.0	69.1
Concrete surface	moulded (M) sandblasted (B) sawn (S)	sawn (S)

where W, C and S are the masses of free water, cement and silica fume powder.

The degradation of the smooth moulded surface MB75-2, shown in the plot at the top in Fig. 8(a), can be characterized as follows: compaction air-voids open and cement paste is abraded to a depth of approximately 0.13 mm. The opening of the air-voids affected the surface asymmetry (R_{sk}) making it (more) negative. Both the air-voids and the abrasion of cement paste increased the roughness (Ra) of the surface measured after the test.

The sand–blasted surface sample BB75-1, second scan from top in Fig. 8(a) and second scan from the left in Fig. 8(b) has many open airvoids and a higher roughness, due to the blasting. The visual impression of surface scans after the 3 km of abrasion test in Fig. 8 (b) shows that the sandblasted sample (BB75-1) has higher roughness and more open air-voids than the moulded surface.

The sawn surfaces of both normal-weight concrete (SB75-1) and lightweight concrete (SLB60) were initially smooth with open air-voids (Fig. 8(a)). After abrasion testing, they were both characterized with protrusion of aggregates (granite in normal-weight aggregate and Stalite in lightweight aggregate, LWA). This can be seen in both the profiles in Fig. 8 (a) and the surface scans in Fig. 8(b). Some of these protrusions presumably resulted from initial valley formation in the paste around coarse aggregates, but Fig. 8(a) shows that protruding LWAs were also worn during the test (SLB60-1), and rather more than the normal-weight aggregate in the SB75-1 sample.

The visual impression of the results in Fig. 8 is that abrasion of the sawn surfaces is greater, that the roughness of the abraded surface is greater, and the skewness is (more) negative due to ice abrasion. In the case of sample SLB60-1, the initial skewness became even more negative due to large dominant air-voids, and the abraded surface had more valleys, and in this specific profile (Fig. 8(a)) the skewness increased.

3.3. Roughness parameters and abrasion rate

Fig. 9 shows the roughness parameters described in Section 2.2 and the abrasion rates for all types of surface during the abrasion test. These are all shown as averages of values detected within the central band (Fig. 2 (b)) for each kilometre of concrete-ice abrasion testing.

Fig. 9(a) shows the concrete-ice abrasion rate during the testing of each surface. As mentioned in the introduction, a severe-to-mild wear transition was observed for all types of concrete surface. The maximum wear rate corresponds to the first kilometre of sliding distance and afterwards reduces substantially. The highest abrasion rate is found for sawn surfaces of lightweight concrete.

Among the different surfaces of concrete mix B75, the highest abrasion rate is seen on the sawn surfaces. As was observed earlier, the abrasion rate of the actual HPC is low, and the differences in abrasion rate between moulded, sawn and sand blasted surfaces are perhaps not discernible. However, the average initial wear rate is higher for moulded surfaces than for sandblasted.

Fig. 9 (b) shows the change of surface roughness during the testing. The results show good reproduction between parallel pairs of samples. The initial roughness data before the test are in good agreement with the visual impression in Fig. 4. As would be expected, the initial roughness of both sawn and moulded surfaces is low and similar to each other, whereas it is higher for the "rough" sandblasted surfaces. The initial roughness of sawn surfaces is higher than for moulded, due to the opened compaction air-voids, and also some aggregate porosity in the case of LWA.

After 3 km of concrete-ice abrasion testing, the roughness of all the concrete surfaces had increased. All samples of the B75 concrete mix show that the initial difference in surface roughness has been reduced over 3 km of sliding. Compared to the other samples, the change in roughness for sandblasted surfaces was very small.

Fig. 9 (c) shows the change in the skewness of the concrete surfaces. All the samples, except for one lightweight aggregate sample (SLB60-1), showed a decrease in skewness, especially during the severe (runningin) wear of the first sliding kilometre of the test. Sample SLB60-1 had more voids initially, which gave it the lowest initial skewness.

Fig. 9 (d) shows the change in the kurtosis of the concrete surfaces during the test. The kurtosis is the measure of both tails of the distribution. For the normal distribution, the value of kurtosis equals 3. Fig. 9 (d) shows the lowest initial kurtosis for concrete samples with moulded surfaces, which means the

weight of the tails in the distribution is very low, which is in agreement with Fig. 6. For all the other samples, the initial kurtosis value is greater than 3, which means that the weight of the tails in the distribution is higher.

The parallel samples, SLB60-1 and SLB60-2 with lightweight aggregates, show very different skewness and kurtosis before the test (Fig. 9 (c, d)), however, this difference reduced after the sliding tests. The difference in surface parameters before the test is shown in Fig. 10, with more pores and open voids before abrasion in SLB60-1 than in SLB60-2, whereas after 3 km the sliding has created similar topographies in the two parallel samples.

3.4. Roughness measured at sub-microscale

Just a few scans of the lightweight concrete sawn surfaces were made with a 3D optical microscope before and after 3 km of ice abrasion testing. Table 2 shows the results for the roughness parameters. Fig. 11 gives pictures from the high-resolution scans. Interestingly, the roughness parameters are affected in the same manner as on the mesoscale, and principally also on the macro scale with the Huovinen's protrusion effect on the large aggregate particles [4]. The effect of ice abrasion was of the same kind and on the same order of magnitude for the normal density concrete. So, even though very small areas were studied, it seems that there is a similar effect of ice abrasion on roughness development over several scales.

3.5. Abrasion of mortars and coarse aggregates (granite and LWA)

The abrasion rates for coarse aggregates and mortars were measured using the visual method described in Section 2.2. The profiles for coarse aggregates and paste were manually selected. Approximately 50% of the data in the narrow central band was classified as either coarse aggregates (28% for B75 and 31% for LB60) or paste (15% for both B75 and LB60). That gave an aggregate surface fraction of 65% for the B75 mix (whereas the real, mixed-in, aggregate volume is 72%) and 68% for the LB60 mix (where the real, mixed-in, aggregate volume is 69%).

Table 2
Roughness parameters of sawn lightweight concrete (LB60) measured with a 3D optical microscope.

	R_a, μm	R_{sk}	R_{ku}
SLB60 (0 km)	8061	−0.392	3.036
SLB60 (3 km)	45.726	−0.969	4.218

Fig. 12 shows the average abrasion rates of coarse aggregates, paste, and concretes within the narrow central band during testing. The abrasion rate is greatest for the paste, and smallest for the aggregates. The lightweight aggregate suffered more abrasion than the normalweight aggregate. Theoretically, the concrete curve should be a weighted average of mortar and aggregate abrasion rates in Fig. 12. The merge of two curves in Fig. 12 (right) is presumably related to the fact that, only 50% of data in the narrow band was classified as aggregate or paste, whereas for the concrete fraction all data was used. So, unclassified visual data seemed to be critical, and could make the concrete curve be a more representative average of paste and aggregate abrasion rates in Fig. 12 (right).

Fig. 13 shows part of the surface scan before and after 3 km testing, which shows the normal-weight aggregate and lightweight aggregate. The surfaces before the test look smooth which is in agreement with profile plots of sawn surfaces before the test in Fig. 8 (a). The surfaces of abraded samples show clear protrusion of aggregates.

3.6. Concrete and ice wear particles

Fig. 14 shows wear particles collected during 3 km of concrete-ice abrasion testing on sawn surfaces B75. The wear particles include cement particles and fine aggregates. The particle size was close to and below 250 μm. The particles have sharp and irregular angular shapes. We did not observe particles in the ice surface after the test, during the change of ice sample. The wear particles were only seen on the concrete surface. We assume, that the wear particles were either continuously removed from the contact zone, or deposited in the valleys on the concrete surface, or rubbed between ice and concrete. The last one would have the largest effect on the abrasion mechanism, as a threebody wear.

Fig. 15 (a) shows typical ice fragments of various sizes and shapes, collected after concrete-ice abrasion testing. The size distribution of ice fragments (Fig. 15 (b)) shows that the majority of fragments are within the range of 4–8 mm.

4. Discussion

To summarize the results given in Section 3, they show that concrete-ice abrasion mostly takes the form of valley formation resulting from either air voids opening or aggregate protrusion and cutting of the peaks. All types of surface show that after abrasion testing the symmetry of the surface roughness has changed towards the negative direction. In general, except for increased wideness and lost height due to the abrasion, the shape of the distribution function was not changed dramatically. In other words, based on the amplitude distribution functions (Fig. 6) within the central band (10 × 127 mm), the concrete surface did not suffer the kind of catastrophic damage that could create a completely different height distribution after the testing.

The roughness parameters (roughness and skewness) are affected in the same manner at both mesoscale (Fig. 9) and microscale (Table 2), and principally also at the macroscale with the protrusion effect of large aggregate particles (Figs. 8 (b), 13). Interestingly, the surface topography somehow seems to be affected in a similar way at three very different scales. A model of abrasion mechanisms therefore needs to account for this multiscale effect. The results after 3 km of testing show the roughness increasing and converging. However, the theoretical detachment of protrusions of coarse aggregate could lead to a dramatic increase in roughness at macroscale.

The normalized amplitude distribution functions (Fig. 7) show that all four specimens (especially SB75-1 and MB75-1) became steeper for the upper 10% of the heights (as indicated with the arrow). This means that peaks are cut. The sawn and moulded surfaces of B75 samples have clear cutting of peaks, and the sawn and sandblasted surfaces have clear formation of valleys. Further sliding testing (from 1 to 3 km, in mild wear mode) does not show clear changes in the normalized amplitude distribution functions. This is most evident for the moulded and sandblasted concrete surfaces. This is surprising and suggests that the mild concrete ice abrasion works similarly over a wide range of asperity sizes. The stable distribution of normalized heights after the first sliding kilometre, can be explained by the increasing contact area between ice and concrete after the first kilometre (excluding local high pressure due to ice fragments and concrete wear particles), through the valley formation, the cutting of peaks, and the water lubricant. The few observations we made with the 3D optical microscope also suggest an increase in roughness at sub-microscale. If we also consider Huovinen's macroscale model with the development of protruding aggregate particles due to ice abrasion, it seems that the roughness increases over a wide range of asperity sizes from sub-micron to centimetres.

The running-in process is either the flattening of surface asperities with further change of symmetry towards the negative valleys, or degradation of the weakest regions (weakest due to compaction voids or the paste or bond zones between aggregate and paste). It is worth to notice, that all tested surfaces got mechanical treatment, this could theoretically cause micro damage of the top surface layer, and result in running-in wear afterwards. The wear rate in the

mild state deviates less than during severe wear. However, the authors are aware of the fact that steady state has not been reached within three kilometres

Fig. 14. Wear particles from sawn concrete surface B75. (Fibres came from filtration paper).

and varies within the central band. Furthermore, mild abrasion is concentrated in the same spots as severe abrasion but with a lower rate. In the case of sawn surfaces, the abrasion is localized in the bond zone between mortar and coarse aggregates (Fig. 8.). This can be related either to the mechanical properties in the interfacial transition zone (ITZ) or to uneven stress distribution due to the different phases of concrete in the concrete-ice contact zone resulting in stress concentration. So, the ITZ seems to be a weak point for the onset of wear, and it would be interesting to make a closer study of the evolution of the abrasion there, perhaps with the 3D optical microscope.

Sawn lightweight concrete samples were found to abrade more than normal-weight concrete. The explanation is the high abrasion of lightweight aggregate compared to granite. The abrasion of paste around the aggregate is also greater for lightweight concrete, which can be explained by the higher porosity of lightweight concrete. Although the water-to-cement ratios of the B75 and LB60 mixes are similar, the porosity of the paste in the LWC is greater due to the air-entraining agent (Table 1).

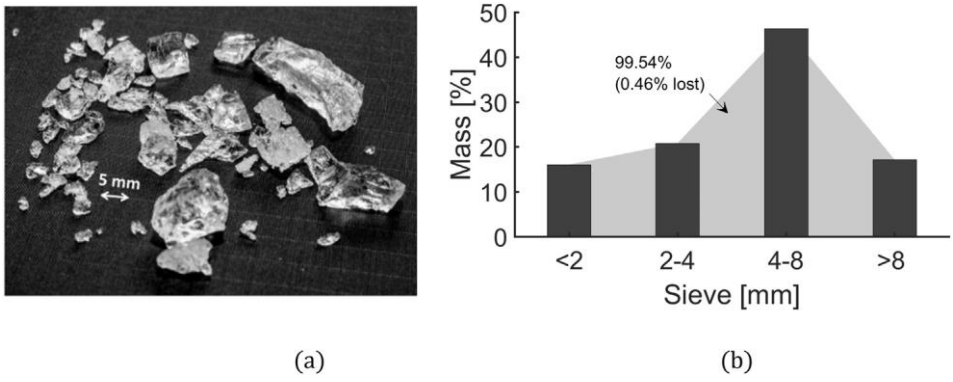

Fig. 15. (a) Ice fragments; (b) ice fragment size distribution.

Although the surfaces changed during the wear process, we could not detect any difference in COF over all 3 km of sliding test [15]. We think that the stable and low value of COF can be explained by a thin water film in the contact area, which works as a lubricant. As previously described, the temperature in the contact zone between ice and concrete was around −2 °C and the coefficient of kinetic friction was around 0.02, which is in agreement with Spagni et al. [31]. Where the thickness of the water film is less than the surface roughness, there is contact between two solids, but otherwise the lubricant coexists with the solid surface or the lubricant supports all the load. However, the mixed lubrication regime is unavoidable at the ends of the sliding path, due to the reciprocal motion of the ice sample.

The wear particles of concrete collected from the sawn surface could theoretically be deposited in the surface valleys and create a protection layer [21]. However, that was not observed, perhaps due to the wet contact, and we abrasion test. A long-term abrasion test is necessary to investigate the steady state.

Interestingly, the abrasion is not homogeneous all over the sample assume that these concrete wear particles caused thirdbody wear during the contact, tumbling between ice and concrete or held by the ice for a few cycles. The effect of ice contamination with particles of soil and sand has been studied in earlier work and found to increase the abrasion rate [21]. The wear particles of ice and concrete we observed were very different in size, but both have sharp, angular shapes, presumably reflecting brittle fracture. The largest concrete wear particles are less than 250 µm. The smallest ice fragments were less than 2 mm, Fig. 15, (but they were not collected in the air as in Timco and Jordaan [30] and there is a chance that the smallest particles were lost). In addition, this result shows that the size of ice fragments is similar to the size of ice crystals (according to the thin section), as assumed in lattice modelling of the onset of concrete-ice abrasion [14]. This observation could contribute in further studies of load transferring through the contact zone. Both concrete wear particles and concrete roughness (Fig. 8) are much smaller than the ice fragments.

5. Conclusion

Various concrete surfaces of B75 mix were studied to investigate the evolution of the concrete-ice abrasion process. Moreover, the abrasion of both normal and lightweight aggregate concrete was studied on sawn surfaces. Based on these topography studies, we came to the following conclusions:

- Concrete-ice abrasion can be understood as mainly valley formation resulting from either air voids opening, or aggregate protrusion and cutting of the peaks.
- Roughness of concrete surfaces increases and skewness decreases at both meso- and microscale.
- Protrusion of both lightweight and normal density aggregate was observed, presumably due to microscale abrasion starting in the ITZ.
- The abrasion rate of lightweight aggregate is greater than that of normal-weight aggregate.
- The angular concrete wear particles had a maximum size of 250 µm, whereas ice fragments of various sizes (approx. 0–8 mm) were observed, of which the majority (> 80%) were larger than 2 mm and also angular, indicating brittle fracture, and the largest ice asperities correlate to the size of ice crystals.

Acknowledgments

This research formed part of the DaCS project (Durable advanced Concrete Solutions – Design and construction for coastal and Arctic regions, Norway). The financial contribution of the Norwegian Research Council (project 245645) and the partners is gratefully acknowledged. The DaCS project partners are: Kværner AS (project owner), Axion AS (Stalite), AF Gruppen Norge AS, Concrete Structures AS, Mapei AS, Multiconsult AS, NorBetong AS, Norcem AS, NPRA (Statens Vegvesen), Norges Teknisk-Naturvitenskapelige Universitet (NTNU), SINTEF Byggforsk, Skanska Norge AS, Unicon AS and Veidekke Entreprenør AS. Special thanks to Dr. Ing. Kjell Tore Fosså of Kværner.

References

[1] A. Héquette, P. Tremblay, P.R. Hill, Nearshore erosion by combined ice scouring and near-bottom currents in eastern Hudson Bay, Canada, Mar. Geol. 158 (1–4) (1999) 253–266 https://doi.org/10.1016/S0025-3227(98)00164-9.

[2] S. Ducret, H. Zahouani, A. Midol, P. Lanteri, T.G. Mathia, Friction and abrasive wear of UHWMPE sliding on ice, Wear 258 (1–4) (2005) 26–31 https://doi.org/10.1016/j.wear.2004.09.026.

[3] H. Kim, C. Daley, H. Kim, Evaluation of large structural grillages subjected to ice loads in experimental and numerical analysis, Mar. Struct. 61 (2018) 467–502 https://doi.org/10.1016/j.marstruc.2018.06.015.

[4] S. Huovinen, Abrasion of concrete structures by ice, Cement Concr. Res. 23 (1) (1993) 69–82 https://doi.org/10.1016/0008-8846(93)90137-X.

[5] Y. Itoh, Y. Tanaka, A. Delgado, H. Saeki, Abrasion depth distribution of a cylindrical concrete structure due to sea ice movement, Int. J. Offshore Polar Eng. 6 (2) (1996) 144–151.

[6] F. Hara, H. Saeki, M. Sato, Y. Takahashi, Prediction of the degree of abrasion of bridge piers by fresh water ice and the protective measures, Proceedings of the International Conference on Concrete under Severe Conditions: Environment and Loading, 1995, pp. 482–494.

[7] E. Møen, K.V. Høiseth, B. Leira, K.V. Høyland, Experimental study of concrete abrasion due to ice friction – Part II: statistical representation of abrasion rates and simple, linear models for estimation, Cold Reg. Sci. Technol. 110 (2015) 202–214 https://doi.org/10.1016/j.coldregions.2014.10.007.

[8] A.T. Bekker, T.E. Uvarova, E.E. Pomnikov, A.E. Farafonov, I.G. Prytkov, R.S. Tyutrin, Experimental study of concrete resistance to ice abrasion, Proceedings of the 21st International Offshore and Polar Engineering Conference, 2011.

[9] M. Hanada, M. Ujihira, F. Hara, H. Saeki, Abrasion rate of various materials due to the movement of ice sheets, Proceedings of the 6th International Offshore and Polar Engineering Conference, 1996.

[10] B. Fiorio, Wear characterisation and degradation mechanisms of a concrete surface under ice friction, Constr. Build. Mater. 19 (5) (2005) 366–375 https://doi.org/10.1016/j.conbuildmat.2004.07.020.

[11] E. Møen, K.V. Høiseth, B. Leira, K.V. Høyland, Experimental study of concrete abrasion due to ice friction – Part I: set-up, ice abrasion vs. material properties and exposure conditions, Cold Reg. Sci. Technol. 110 (2015) 183–201 https://doi.org/10.1016/j.coldregions.2014.09.008.

[12] J. Tijsen, S. Bruneau, B. Colbourne, Laboratory examination of ice loads and effects on concrete surfaces from bi-axial collision and adhesion events, Proceedings of the International Conference on Port and Ocean Engineering under Arctic Conditions, POAC, 2015.

[13] S. Jacobsen, G.W. Scherer, E.M. Schulson, Concrete-ice abrasion mechanics, Cement Concr. Res. 73 (2015) 79–95 https://doi.org/10.1016/j.cemconres.2015.01.001.

[14] N. Ramos, G. Shamsutdinova, M.A.N. Hendriks, S. Jacobsen, Lattice modelling of the onset of concrete-ice abrasion, 8th International Conference on Concrete under Severe Conditions – Environment and Loading, 2016, pp. 351–358.

[15] G. Shamsutdinova, M.A.N. Hendriks, S. Jacobsen, Concrete-ice abrasion: wear, coefficient of friction and ice consumption, Wear 416–417 (2018) 27–35 https://doi.org/10.1016/j.wear.2018.09.007.

[16] E. Horszczaruk, Mathematical model of abrasive wear of high performance concrete, Wear 264 (1–2) (2008) 113–118 https://doi.org/10.1016/j.wear.2006.12. 008.

[17] Y. Itoh, Y. Tanaka, H. Saeki, Estimation method for abrasion of concrete structures due to sea ice movement, Proceedings of the 4th International Offshore and Polar Engineering Conference, 1994.

[18] G. Liang, S. Schmauder, M. Lyu, Y. Schneider, C. Zhang, Y. Han, An investigation of the influence of initial roughness on the friction and Wear behavior of ground surfaces, Materials (Basel) 11 (2) (2018) 237 https://doi.org/10.3390/ ma11020237.

[19] S.K. Chilamakuri, B. Bhushan, Contact analysis of non-Gaussian random surfaces, Proc. IME J. J. Eng. Tribol. 212 (1) (1998) 19–32 https://doi.org/10.1243/ 1350650981541868.

[20] J.-H. Horng, M.-L. Len, J.-S. Lee, The contact characteristics of rough surfaces in line contact during running-in process, Wear 253 (9–10) (2002) 899–913 https://doi.org/10.1016/S0043-1648(02)00025-X.

[21] M. Federici, G. Perricone, S. Gia lamella, G. Straffelini, Sliding behaviour of friction material against cermet coatings: pin-on-disc study of the running-in stage, Tribol. Lett. 66 (2) (2018) 53 https://doi.org/10.1007/s11249-018-1004-3.

[22] F.D. Rzatki, D.V.D. Barboza, R.M. Schroeder, G.M. de O. Barra, C. Binder, A.N. Klein, J.D.B. de Mello, Effect of surface finishing, temperature and chemical ageing on the tribological behaviour of a polyether ether ketone composite/52100 pair, Wear 332–333 (2015) 844–854 https://doi.org/10.1016/j.wear.2014.12.035.

[23] G. Dai, F. Pohlenz, A. Felgner, H. Bosse, H. Kunzmann, Quantitative analysis of nano-wear on DLC coatings by AFM, CIRP Ann. - Manuf. Technol. 62 (1) (2013) 543–546 https://doi.org/10.1016/j.cirp.2013.03.022.

[24] S. Panda, S.K. Roy Chowdhury, M. Sarangi, Effects of non-Gaussian counter-surface roughness parameters on wear of engineering polymers, Wear 332–333 (2015) 827–835 https://doi.org/10.1016/j.wear.2015.01.020.

[25] H. Gao, G.C. Barber, M. Shillor, Numerical simulation of engagement of a wet clutch with skewed surface roughness, J. Tribol. 124 (2) (2002) 305–312.

[26] G. Shamsutdinova, M.A.N. Hendriks, S. Jacobsen, Concrete-ice abrasion test with sliding ice and ice spallation, Nord. Concr. Res. 57 (2017) 39–57.

[27] ISO 4287 Geometrical Product Specifications (GPS), Surface Texture: Profile Method – Terms, Definitions and Surface Texture Parameters, (1997).

[28] EN 12350-1, Testing Fresh Concrete. Sampling, (2009).

[29] EN 206:2013+NA:2014, Concrete – Specification, Performance, Production and Conformity – National Annex, (2014).

[30] G.W. Timco, I. Jordaan, Time-series variations in ice crushing, Proceedings of the 9th Conference of Port and Ocean Engineering under Arctic Conditions, 1987.

[31] A. Spagni, A. Berado, D. Marchetto, E. Gualtieri, N.M. Pugno, S. Valeri, Friction of rough surfaces on ice: experiments and modeling, Wear 368–369 (2016) 258–266 https://doi.org/10.1016/j.wear.2016.10.001.